Publication Year	2022
Acceptance in OA	2025-02-26T16:48:44Z
Title	Weak Mass Loss from the Red Supergiant Progenitor of the Type II SN 2021yja
Authors	Hosseinzadeh, Griffin, Kilpatrick, Charles D., Dong, Yize, Sand, David J., Andrews, Jennifer E., Bostroem, K. Azalee, Janzen, Daryl, Jencson, Jacob E., Lundquist, Michael, Meza Retamal, Nicolas E., Pearson, Jeniveve, Valenti, Stefano, Wyatt, Samuel, Burke, Jamison, Hiramatsu, Daichi, Howell, D. Andrew, McCully, Curtis, Newsome, Megan, Gonzalez, Estefania Padilla, Pellegrino, Craig, Terreran, Giacomo, Auchettl, Katie, Davis, Kyle W., Foley, Ryan J., Miao, Hao-Yu, Pan, Yen-Chen, Rest, Armin, Siebert, Matthew R., Taggart, Kirsty, Tucker, Brad E., Cyrus Leung, Feng Lin, Swift, Jonathan J., Yang, Grace, Anderson, Joseph P., Ashall, Chris, BENETTI, Stefano, Brown, Peter J., Cartier, Régis, Chen, Ting-Wan, DELLA VALLE, Massimo, Galbany, Lluís, Gomez, Sebastian, Gromadzki, Mariusz, Haislip, Joshua, Hsiao, Eric Y., Inserra, Cosimo, Jha, Saurabh W., Killestein, Thomas L., Kouprianov, Vladimir, Kozyreva, Alexandra, Müller-Bravo, Tomás E., Nicholl, Matt, Paraskeva, Emmy, Reichart, Daniel E., Ryder, Stuart, Shahbandeh, Melissa, Shappee, Ben, Smith, Nathan, Young, David R.
Publisher's version (DOI)	10.3847/1538-4357/ac75f0
Handle	http://hdl.handle.net/20.500.12386/36294
Journal	THE ASTROPHYSICAL JOURNAL
Volume	935

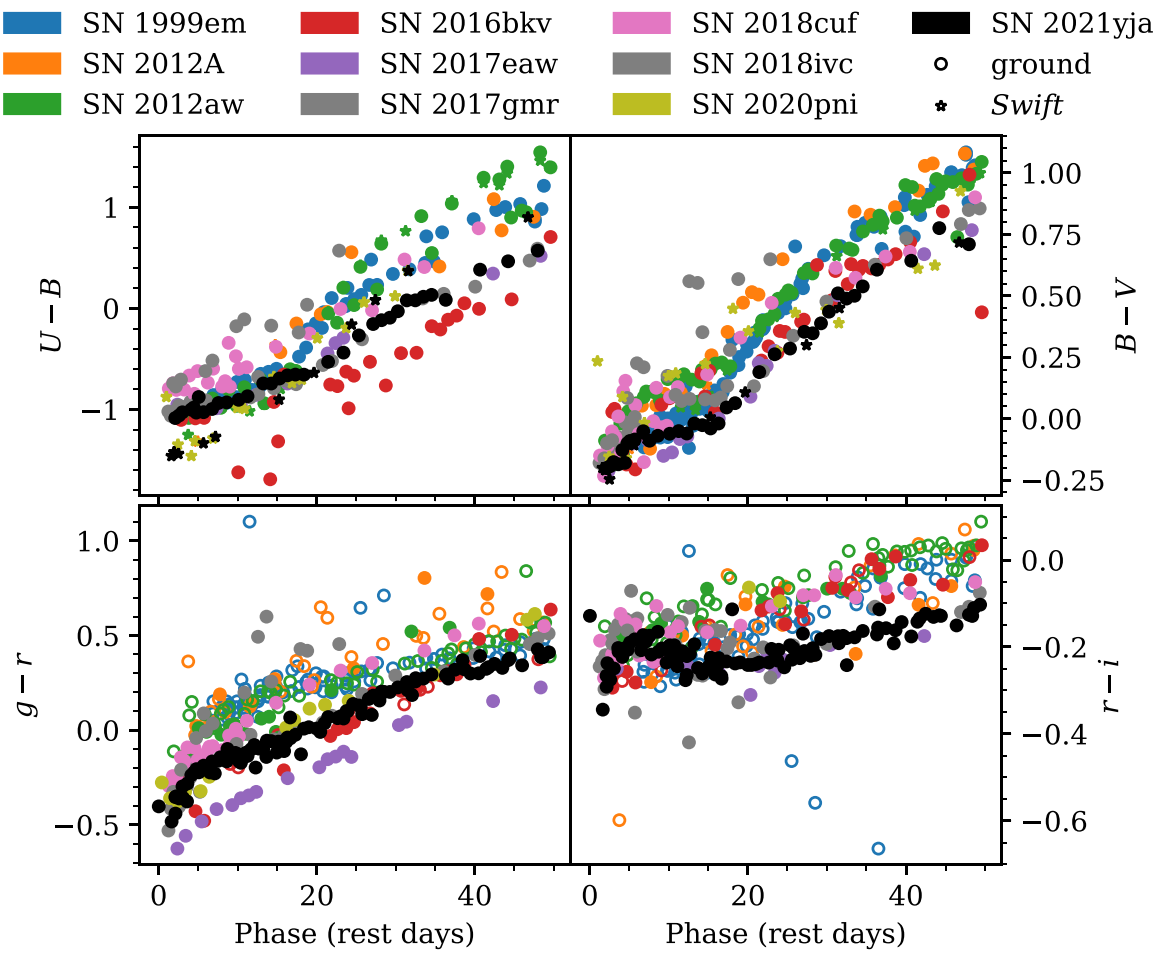

Figure 8. Extinction-corrected color curves of SN 2021yja compared to other SNe II. Open markers for $g-r$ and $r-i$ are converted from $V-R$ and $R-I$, respectively, according to the relationships of Jordi et al. (2006). The bump in the color curves ending around 15 d happens around the same time that a change in plateau slope is commonly observed in SNe II (Anderson et al. 2014), although such a change is not obvious in our light curve. Otherwise, the color evolution of SN 2021yja is fairly typical.

(The data used to create this figure are available.)

Table 3
Shock Cooling Parameters

Parameter	Variable	Prior Shape	Prior	Parameters[a]	Best-fit Value[b]	Units
Shock velocity	v_{s*}	Uniform	0	3	1.0 ± 0.2	$10^{8.5}$ cm s^{-1}
Envelope mass[c]	$M_{\rm env}$	Uniform	0	10	0.6 ± 0.1	$M_\odot$
Ejecta mass × numerical factor[d]	$f_\rho M$	Uniform	3	100	60 ± 30	$M_\odot$
Progenitor radius	R	Uniform	0	100	14 ± 2	10^{13} cm
Distance	d_L	Gaussian	23.4	4.9	25 ± 5	Mpc
Extinction	$E(B-V)$	Gaussian	0.104	0.0155	$0.105^{+0.010}_{-0.009}$	mag
Explosion time	t_0	Uniform	59460	59464.6	59464.40 ± 0.06	MJD
Intrinsic scatter	σ	Half-Gaussian	0	1	4.8 ± 0.2	Dimensionless

Notes.
[a] The "Prior Parameters" column lists the minimum and maximum for a uniform distribution, and the mean and standard deviation for a Gaussian distribution.
[b] The "Best-fit Value" column is determined from the 16th, 50th, and 84th percentiles of the posterior distribution, i.e., median $\pm 1\sigma$.
[c] Sapir & Waxman (2017) define the envelope of an RSG as the region where $\delta \equiv \frac{R-r}{R} \ll 1$, where the density follows $\rho_0(\delta) = \frac{3f_\rho M}{4\pi R^3}\delta^n$ (we adopt $n = \frac{3}{2}$ for convective envelopes).
[d] The ejecta mass and density profile do not have a strong effect on the light curve. Therefore this parameter is essentially unconstrained.

luminosity from ongoing circumstellar interaction, although the decline slope we measure above suggests that ^{56}Co decay is the dominant power source. An unusually large nickel mass may suggest a massive progenitor, according to the correlations of Eldridge et al. (2019). We discuss this possibility further in Section 4.2.

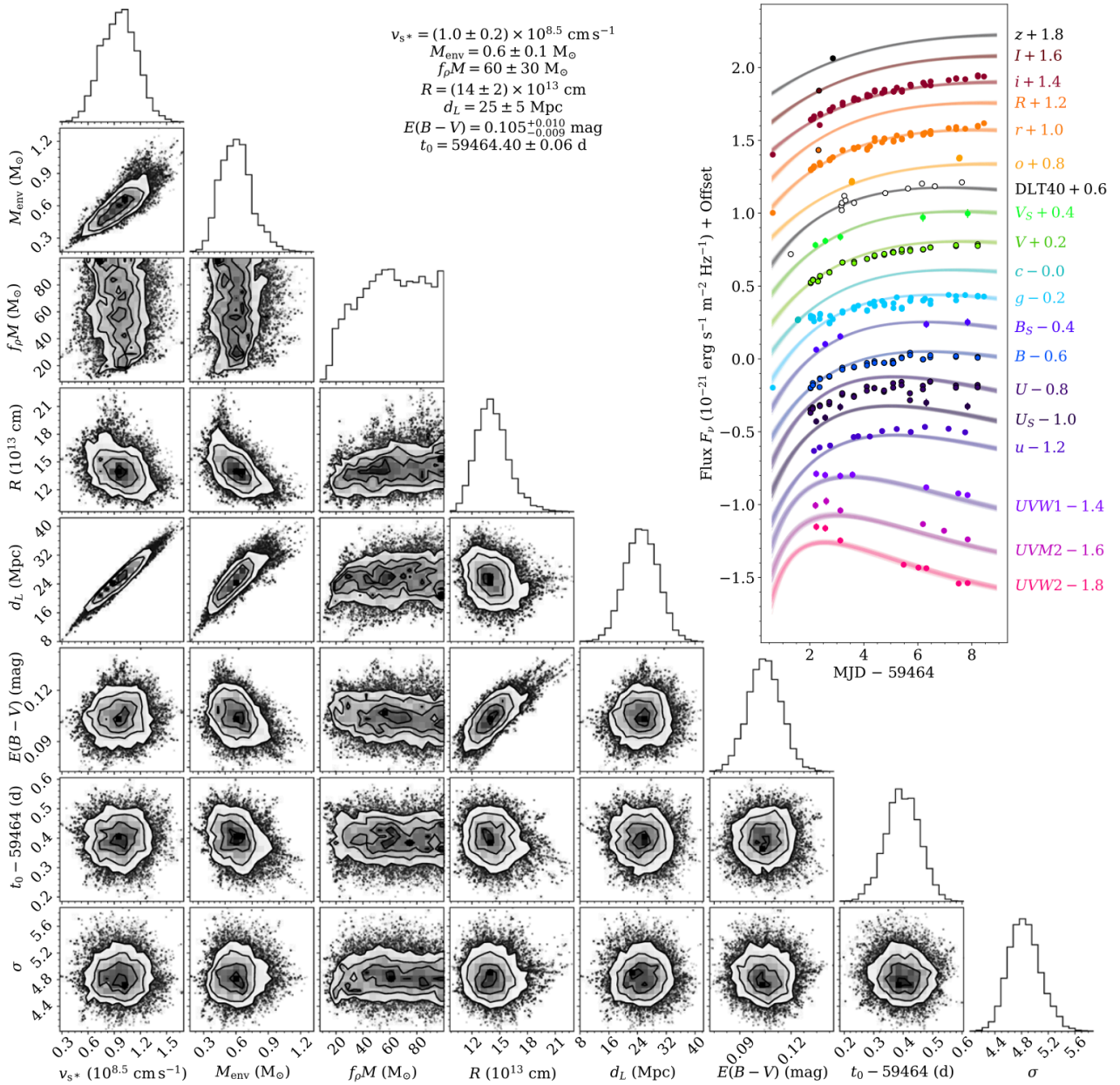

Figure 9. Modeling the shock cooling emission of SN 2021yja using the model of Sapir & Waxman (2017). The parameters are described in Table 3. We find that the first detection with MuSCAT3 occurred 5.4 ± 1.4 rest-frame hours after the best-fit explosion time. We also find the best-fit progenitor radius to be 2030^{+260}_{-230} $R_\odot$. This unusually large radius for an RSG can be lowered if we adopt a smaller extinction value or if we attribute some of the UV flux to interaction with CSM.

(The data used to create this figure are available.)

3.4. Spectral Features

The spectroscopic evolution of SN 2021yja $\gtrsim 6$ days after explosion is typical for a SN II: P Cygni lines of hydrogen and helium superimposed on a cooling blackbody. Metal lines, including Ba II and Fe II begin to appear several weeks after explosion, blanketing the blue side of the spectrum. Its infrared spectra (Figure 4) place it in the "weak" class of Davis et al. (2019), with weak helium absorption at 1.083 μm in our > 100 d spectra, a high-velocity component of the same line, and more pronounced Sr II absorption. As such, SN 2021yja is consistent with the correlation between slow plateau decline rates and weak infrared helium absorption (Davis et al. 2019). No carbon monoxide emission is detected at 100 days after explosion.

However, our earliest optical spectra, taken around 2 days after explosion, are somewhat unusual in the sense that they do not show the narrow high-ionization lines seen in many SNe II this early. These lines indicate short-lived circumstellar interaction, which ends when the nearby circumstellar material (CSM) is swept up by the expanding ejecta (Gal-Yam et al. 2014; Smith et al. 2015; Khazov et al. 2016; Yaron et al. 2017; Bullivant et al. 2018; Hosseinzadeh et al. 2018; Soumagnac et al. 2020; Bruch et al. 2021; Hiramatsu

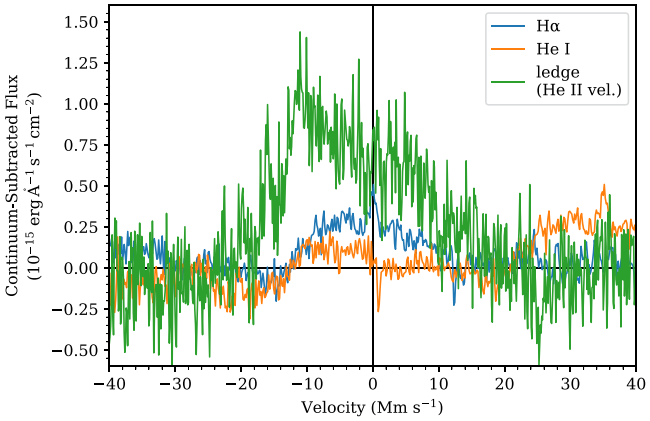

Figure 10. The profile of the unidentified feature around 450–480 nm (green) in the first spectrum of SN 2021yja, compared to the profiles of Hα (blue) and He 587.6 nm (orange). He II could be contributing at 468.6 nm, but the feature is broad and has an irregular shape, unlike the other P Cygni profiles. As suggested by Soumagnac et al. (2020) and Bruch et al. (2021), we suspect this is a combination of several lines, possibly indicating a low level of circumstellar interaction. However, its breadth cannot be fully explained by the handful of narrow flash-ionized lines they suggest.

et al. 2021b; Terreran et al. 2022). Figure 2 compares the early spectra of SN 2021yja to other SNe II with well-constrained explosion dates and high-quality spectra taken within 6 days of explosion. Some show narrow He II, C III, N III, and other lines: SN 2013fs (Yaron et al. 2017; Bullivant et al. 2018), SN 2017ahn (Tartaglia et al. 2021), SN 2018zd (Hiramatsu et al. 2021b), and SN 2020pni (Terreran et al. 2022). SN 2017gmr (Andrews et al. 2019) and SN 2021yja do not show these lines, but instead show a unique "ledge-shaped" feature around 450–480 nm, which we discuss below.

Figure 10 shows a detailed view of the ledge-shaped feature in the earliest spectrum of SN 2021yja, compared to Hα and He 587.6 nm in the same spectrum. There are two lines of thought about the identity of this feature in the literature, both related to circumstellar interaction. Bullivant et al. (2018, their Figure 20) and Andrews et al. (2019, their Figure 18) interpret it as very broad, blueshifted He II 468.6 nm (although there is also a narrow component of this line present) produced in the outermost layers of the SN ejecta. However, the line profile is somewhat more symmetrical in these SNe than in SN 2021yja. Soumagnac et al. (2020, their Figure 7) and Bruch et al. (2021, their Figure 5) interpret this feature as a blend of various flash-ionized lines from the CSM: N V 460.4 and 462.0 nm, N II 463.1 and 464.3 nm, C IV 465.8 nm, and He II 468.6 nm.

Neither of these explanations is fully satisfactory. The former (single, broad line) is difficult to reconcile with the irregular profile of the feature, when other features have typical P Cygni profiles. In addition, the implied velocity is nearly 30,000 km s^{-1} (as measured from the He II rest wavelength to the blue edge of the feature), which is much higher than any other feature in the spectrum. The latter explanation (blend of several narrow emission lines) is inconsistent with the breadth and strength of the feature. We suspect that the feature is indeed a blend of several lines, possibly including He II, C III, and N III, although these must be either much broader or much more numerous than the features suggested by previous work. We discuss one such possibility in Section 4.1.

3.5. Limits on a Pre-explosion Counterpart

Figure 11 (left) shows our high-resolution GSAOI image of SN 2021yja, aligned to the pre-explosion WFPC2 F606W image using three common astrometric sources in both frames, resulting in an rms astrometric uncertainty of 0.08″ (0.8 WFPC2 pixels) between both frames. In addition, we aligned the GSAOI image to DECam and Spitzer/IRAC imaging, using 4–6 common astrometric standards in both frames and resulting in an rms uncertainty of 0.07–0.12″ (Figure 11, right).

The position of SN 2021yja does not align with any counterpart in the HST imaging. The closest source is 0.88″ (11σ) away from this position and detected at $m_{\rm F606W} = 24.05 \pm 0.06$ mag (previously discussed in Kilpatrick 2021). The same is true in each of the other pre-explosion images as shown in Figure 11, with no evidence for any significant, point-like emission within at least 3σ of the site of SN 2021yja.

Motivated by the depth of our imaging set, we place 3σ limits on the presence of a counterpart in each of our pre-explosion images. We estimate the standard deviation of the background variation within 2″ of SN 2021yja and use this value to estimate the maximum total flux that would not be flagged as a 3σ detection within one PSF width at this location. The resulting limits are given in AB mag in Table 4, which we consider the 3σ limits on the presence of any counterpart in each image.

To place these limits in context, we assume a blackbody spectral energy distribution with a given luminosity and show the region of the Hertzsprung-Russell diagram ruled out by our limits assuming a source at 23.4 Mpc and the extinction we derive in Section 2.5. We compare these limits to the expected luminosities and temperatures of single-star models derived from stars in MESA Isochrones & Stellar Tracks (MIST; Choi et al. 2016). We can rule out all stars with initial masses $>9\,M_{\odot}$ as shown in Figure 12. This analysis is dominated by the WFPC2 limit, which is significantly more constraining for the MIST models than DECam and Spitzer.

Thus while we rely on the WFPC2 image from 26 March 1997, 24.5 yr before explosion, for our best constraints on the nature of any progenitor star of SN 2021yja, we can place meaningful constraints on that star at later times when the DECam and Spitzer imaging were obtained. These limits are informative in the scenario where that star was highly variable and had a lower flux in F606W compared to its average flux (i.e., similar to variability in α Ori and the recent detection of a dimming RSG in M51 described in Levesque & Massey 2020; Jencson et al. 2022). We further explore the implications of this scenario below.

4. Discussion

4.1. CSM

Our analysis above gives rise to a somewhat confusing picture with regard to CSM around the progenitor of SN 2021yja. On one hand, we do not see some standard signs of CSM, including pronounced, narrow emission lines in early spectra, and, at first glance, the shock cooling model appears to fit our observed light curve reasonably well. On the other hand, the high UV luminosity, very blue colors, and persistent high temperature (resulting in an overly large progenitor radius from the shock cooling model), as well as the ledge-shaped feature in the early spectra, do suggest some level of early circumstellar interaction. HST UV-optical spectra from

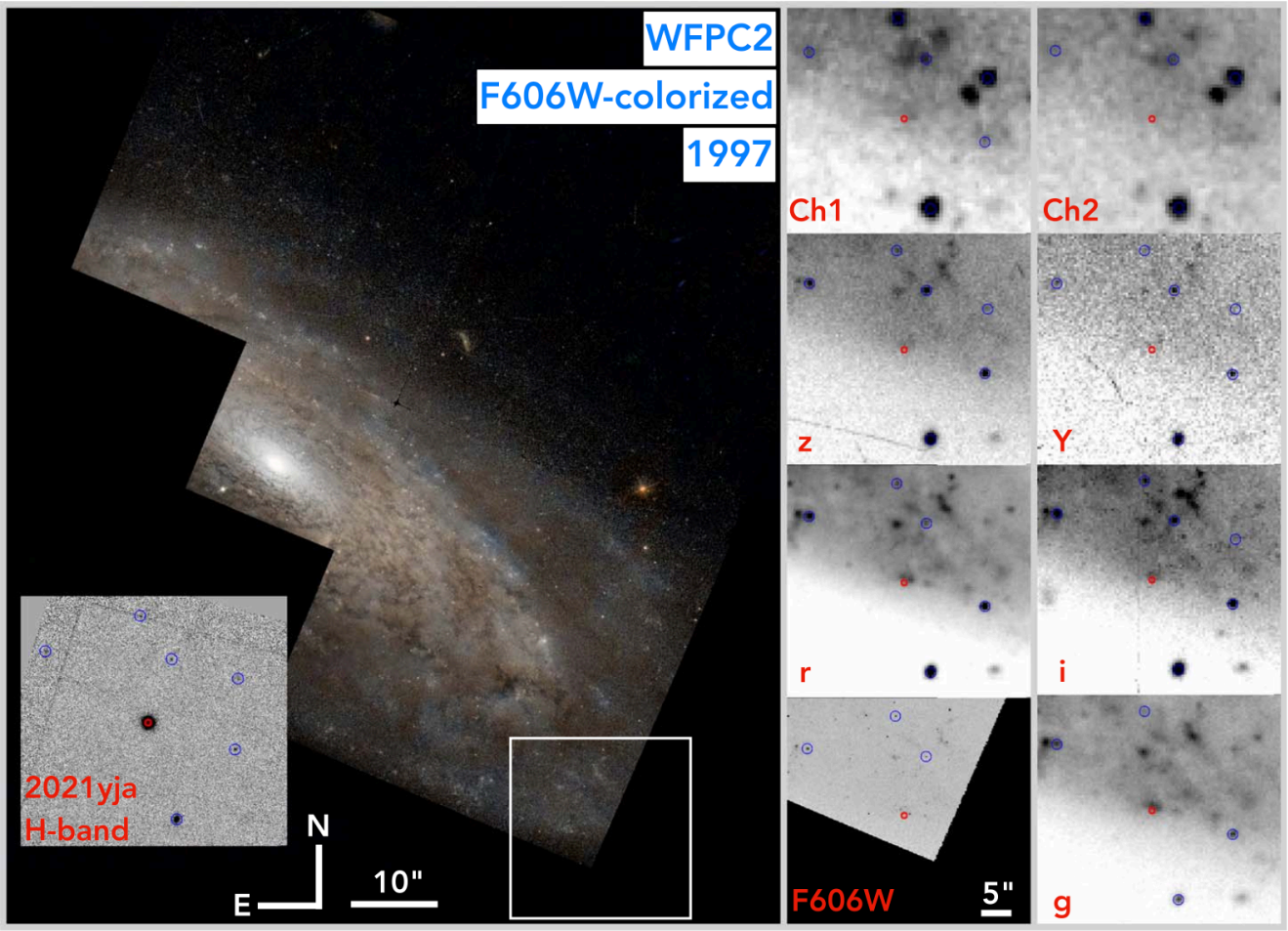

Figure 11. HST/WFPC2 F606W imaging of NGC 1325 from 1997 colorized using DSS imaging of the same field (left) and showing the explosion site of SN 2021yja (white square). An inset panel shows GSAOI imaging of SN 2021yja obtained in Dec. 2021 in a 40″×40″ region corresponding to the white frame. The right-hand panels show the same region as seen in F606W, DECam *grizY*, and Spitzer/IRAC Channel 1 and 2, aligned using 3–6 common astrometric standards (blue circles) and centered on the site of SN 2021yja (red circle). The lack of a counterpart is described in Section 3.5.

Table 4
Limits on a Pre-explosion Counterpart to SN 2021yja

Instrument	Band	Magnitude
WFPC2	F606W	>27.15
DECam	*g*	>24.50
DECam	*r*	>24.08
DECam	*i*	>22.90
DECam	*z*	>22.56
DECam	*Y*	>21.90
Spitzer/IRAC	Ch 1	>22.60
Spitzer/IRAC	Ch 2	>22.20

Note. All limits are given in AB magnitudes as described in Section 3.5.

Vasylyev et al. (2022) show no sign of circumstellar interaction, but these were observed much later (7 days after explosion) than our early spectra showing the ledge. In addition, the detection of delayed radio emission (Alsaberi et al. 2021) from SN 2021yja following an initial non-detection (Ryder et al. 2021) can be taken as an indication of interaction with a non-uniform CSM, similar to the conclusion of Bostroem et al. (2019) for the SN II ASASSN-15oz. SN 2021yja was also observed in the very high-energy γ-ray domain ($E > 100$ GeV) by the High Energy Stereoscopic System (H.E.S.S.) Imaging Atmospheric Cherenkov Telescope Array, which will yield complementary constraints on the CSM density (H.E.S.S. Collaboration 2022, in preparation) following the work presented by Abdalla et al. (2019) and the H.E.S.S. Collaboration (2022).

One way to resolve this apparent contradiction is to infer a small amount of CSM: less than is required to produce strong emission lines, but still enough to affect the broadband light curve, especially in the UV. We turn to the literature to constrain the mass-loss rate from both directions. By modeling a sample of early SN II spectra with narrow emission lines, Boian & Groh (2020) find CSM density parameters of order $D \sim 10^{15-16}$ g cm^{-1}, corresponding to mass loss of $\dot{M} \equiv 4\pi v_\infty D \gtrsim 10^{-4}\ M_\odot \mathrm{yr}^{-1}$, where v_∞ is the terminal wind speed. Our mass-loss rate must therefore be $\dot{M} \lesssim 10^{-4}\ M_\odot \mathrm{yr}^{-1}$.

Dessart et al. (2017) propose a scenario in which the interaction lines are both broadened and blueshifted, which can potentially explain the ledge-shaped feature we discuss in Section 3.4. This occurs when an RSG with radius $R_\star = 501\ R_\odot$ explodes into low-density CSM ($\dot{M} = 10^{-6}\ M_\odot \mathrm{yr}^{-1}$). They term this the `r1w1` model. In this scenario, narrow emission lines are not seen or disappear within hours of explosion, at

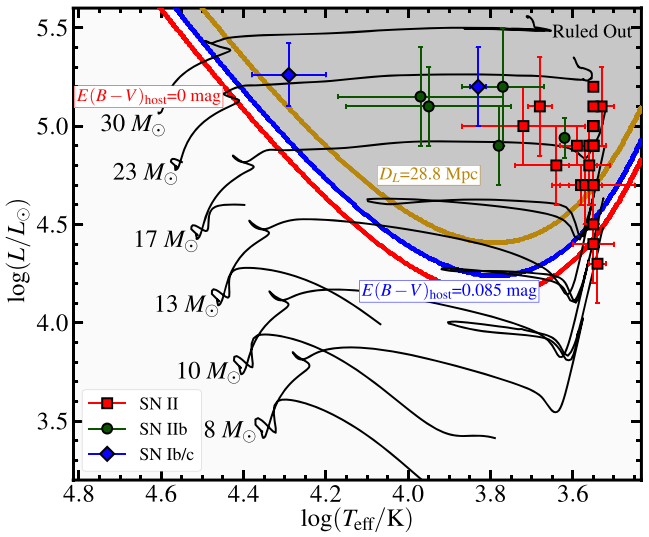

Figure 12. Hertzsprung-Russell diagram showing the region that is ruled out for a counterpart to SN 2021yja by our limits in Table 4 (red line) and assuming $E(B-V)_{\rm host}=0.0$ mag and $D_{\rm host}=23.4$ Mpc. For comparison, we show the same limits using the updated reddening value of $E(B-V)_{\rm host}=0.085$ mag and a total-to-selective extinction ratio of $R_V=3.1$ (blue), and the limits assuming this reddening and a farther distance of 28.8 Mpc (gold; assumed distance + 1σ). We also overplot MIST single-star evolutionary tracks for stars with initial masses 8–30 $M_\odot$ (black lines) as well as counterparts to Type Ib, IIb, and II SNe from the literature (Cao et al. 2013; Smartt 2015; Kilpatrick et al. 2021, and references therein). For our fiducial host distance and reddening values, our limits rule out evolved massive stars $>9\,M_\odot$.

which time we had not yet observed the spectrum of SN 2021yja. When they add an extended atmosphere onto the RSG (`r1w1h` model; scale height $H_\rho=0.3R_\star$), the spectroscopic evolution is similar, but the light curve rises faster and is much more luminous in the UV (reaching $M_{UVW2}\approx-19.5$ mag). Such an extended atmosphere only requires a small energy injection during the last year before explosion (Smith & Arnett 2014; Morozova et al. 2020). Figure 13 compares the early spectra of SN 2021yja to the `r1w1` and `r1w1h` models of Dessart et al. (2017). Notably, the extended atmosphere or `r1w1h` could also lead to an overestimate of the progenitor radius by a shock cooling model that was not designed to account for it. Therefore, we believe this to be the most likely scenario for the progenitor of SN 2021yja: an RSG with an extended atmosphere exploding into low-density CSM.

4.2. Progenitor Star

Because of our skepticism about the inferred progenitor radius (Section 4.1), the best constraints we have on the progenitor are (1) the luminosity limit from direct imaging of the field before explosion and (2) the inferred nickel mass from the light-curve tail. Unfortunately, these are also somewhat in conflict with each other: the very strict luminosity limit suggests a very low-mass progenitor (with some caveats, discussed below), whereas the very large nickel mass suggests a massive progenitor ($\gtrsim 20\,M_\odot$; Eldridge et al. 2019). The latter places SN 2021yja close to the upper limit for SN II progenitors (Smartt 2015; Davies & Beasor 2018, 2020a, 2020b), implying that its progenitor star ought to have $M_V=-5$ to -6 mag.

The limits from WFPC2 suggest that $M_V>-4.4$ mag, consistent with a progenitor star of initial mass $<9\,M_\odot$ (and following the single-star models of Choi et al. 2016). We consider this a credible limit on the initial mass of the progenitor star derived using the same distance and extinction assumptions as SN 2021yja above, but we acknowledge that there is some tension with the nature of the progenitor star as inferred from the SN light curve. Our pre-explosion limit is dominated by the single epoch of WFPC2/F606W imaging from 1997, 24.5 years before explosion, which provides the deepest limits. The tension between our pre-explosion constraints on the progenitor star and those derived from SN 2021yja could be partly eased if the star were extinguished or variable on timescales of decades before core collapse.

A -0.6 to -1.4 mag discrepancy between this expectation and our derived limits could be explained by variability in the progenitor star V-band magnitude confined to a single epoch 24.5 yr prior to core collapse, similar to the variability observed in RSGs such as Betelgeuse and M51-DS1 (Levesque & Massey 2020; Jencson et al. 2022). The peak-to-peak variability in Betelgeuse was $\approx$1.2 mag such that even a fraction of this change in the SN 2021yja progenitor star would completely obscure a $<15\,M_\odot$ star in our WFPC2/F606W imaging. We note, however, that these are extreme cases, and evidence from RSGs observed in M31 (Soraisam et al. 2018) and M51 (Conroy et al. 2018) suggests that the vast majority of RSGs in the expected luminosity range for the SN 2021yja progenitor star do not exhibit such extreme variability. Indeed, assuming that all RSGs follow similar V- and I-band variability to that observed in M51, those observed in Conroy et al. (2018) suggest that $<8\%$ of those stars will undergo peak-to-peak dimming at $M_I>-0.6$ mag. However, this likelihood is highly uncertain for RSGs as a whole, and in particular, those that are <25 yr from core collapse, which may be even more variable than the overall population (e.g., Jacobson-Galán et al. 2022).

Alternatively, the CSM discussed above could significantly obscure the progenitor star in F606W if it contained a significant dust mass. Assuming Beasor et al. (2020) mass-loss rates for an RSG in this mass range ($\approx 10^{-6}\,M_\odot$ yr) and corresponding wind speeds (20–25 km s^{-1}), we consider the implied effect on circumstellar extinction. Following methods in Kilpatrick et al. (2018) for a uniform wind with carbonaceous dust grains, we infer that SN 2021yja would experience a line-of-sight extinction $A_V\approx0.1$ mag, in which case circumstellar extinction could not explain an anomalously low optical luminosity for the SN 2021ya progenitor star. However, we note that this is strongly dependent on the assumed mass-loss rate and wind composition, which could be significantly different.

5. Summary and Conclusions

We have presented high-cadence, early photometric and spectroscopic observations of the Type II SN 2021yja. These have conflicting interpretations with respect to the progenitor star and its CSM. On one hand, the light curve is very luminous, especially in the UV, but on the other hand, we see no narrow emission lines in the early spectra. The high luminosity on the radioactive-decay tail of the light curve also implies a large production of ^{56}Ni (though with a large uncertainty), which suggests a large progenitor mass. However, we inspected archival HST imaging of the host galaxy of SN 2021yja and found no coincident sources that could be the progenitor. If stellar evolution models accurately describe the end state of stars, these limits suggest the progenitor was among the lowest-mass RSGs, $\lesssim 9\,M_\odot$.

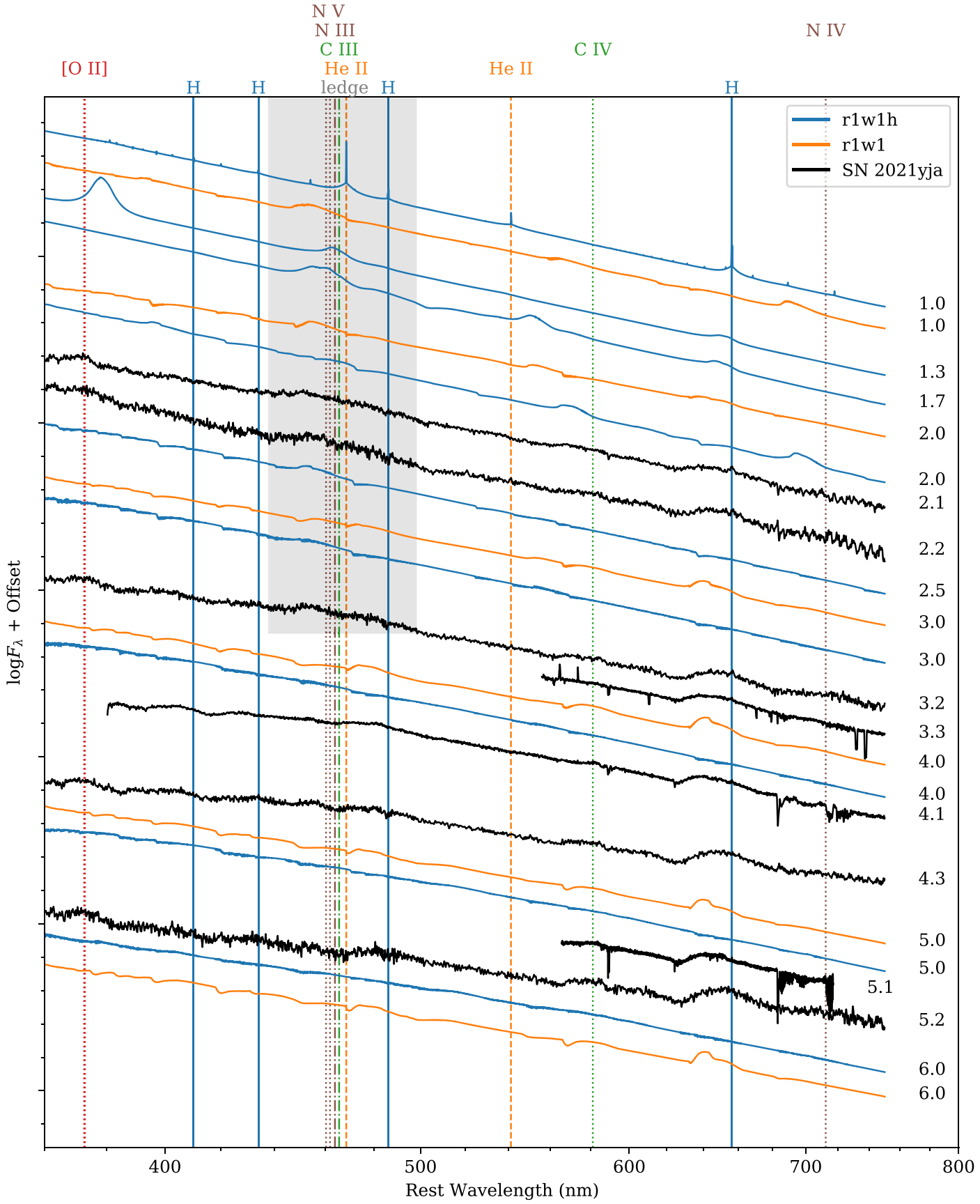

Figure 13. Comparing the early spectra of SN 2021yja to the `r1w1` and `r1w1h` models of Dessart et al. (2017), with lines labeled as in Figure 2. These models both have low-density CSM from a mass-loss rate of order $\dot{M} \approx 10^{-6}\ M_\odot \mathrm{yr}^{-1}$. The `r1w1h` model also includes an extended RSG atmosphere. Although not a perfect match to the models, the ledge-shaped feature we observe around 450–480 nm could be explained by weak circumstellar interaction, in particular by broad, blueshifted He II and N V.

We conclude that the most likely progenitor is an RSG with an extended envelope, and that this progenitor exploded into low-density CSM produced via a mass-loss rate of order $\dot{M} \sim 10^{-6}\ M_{\odot}\ \mathrm{yr}^{-1}$. This CSM still has observable effects on the light curve and spectra. We emphasize that the details of the progenitor structure and CSM configuration must be considered in analyzing CCSNe; these lead to a multidimensional phase space of observables, i.e., a "zoo" of spectral features that do not map straightforwardly onto mass-loss rate or CSM density.

As we discover CCSNe increasingly early, thanks to specially designed survey strategies, detailed modeling of each well-observed event will allow us to piece together the statistics of the CCSN progenitor population. In particular, combining multiple independent lines of analysis, e.g., light-curve modeling, spectral modeling, and direct progenitor imaging, will allow us to build a complete picture of each new event, including mass-loss history, CSM density and composition, and progenitor structure. With a sample of well-studied events, we will gain a comprehensive view of the diversity of mass loss in massive stars in their final years.

We thank Luc Dessart for providing his model light curves and spectra and for insightful comments on the manuscript; Maria Jose Bustamante, Samaporn Tinyanont, César Rojas-Bravo, David Jones, and Kayla Loertscher for their effort in taking Kast data; UCSC undergraduates Cirilla Couch, Jessica Johnson, Payton Crawford, Srujan Dandu, and Zhisen Lai for their effort in taking Nickel data; Rosalie McGurk, Vivian U, and Tianmu Gao for obtaining the KCWI spectrum; and Andrew Howard and Howard Isaacson for reducing the HIRES spectrum.

Some of the data presented herein were obtained at the W. M. Keck Observatory, which is operated as a scientific partnership among the California Institute of Technology, the University of California, and the National Aeronautics and Space Administration. The Observatory was made possible by the generous financial support of the W. M. Keck Foundation. This research has made use of the Keck Observatory Archive (KOA), which is operated by the W. M. Keck Observatory and the NASA Exoplanet Science Institute (NExScI), under contract with the National Aeronautics and Space Administration. The authors wish to recognize and acknowledge the very significant cultural role and reverence that the summit of Maunakea has always had within the indigenous Hawai'ian community. We are most fortunate to have the opportunity to conduct observations from this mountain. Based on observations obtained at the international Gemini Observatory, a program of NSF's NOIRLab, which is managed by the Association of Universities for Research in Astronomy (AURA) under a cooperative agreement with the National Science Foundation. on behalf of the Gemini Observatory partnership: the National Science Foundation (United States), National Research Council (Canada), Agencia Nacional de Investigación y Desarrollo (Chile), Ministerio de Ciencia, Tecnología e Innovación (Argentina), Ministério da Ciência, Tecnologia, Inovações e Comunicações (Brazil), and Korea Astronomy and Space Science Institute (Republic of Korea). Based on observations collected at the European Organisation for Astronomical Research in the Southern Hemisphere, Chile, as part of ePESSTO+ (the advanced Public ESO Spectroscopic Survey for Transient Objects Survey). ePESSTO+ observations were obtained under ESO programs ID 1103.D-0328 and 106.216C (PI: Inserra). Based in part on observations obtained at the Southern Astrophysical Research (SOAR) telescope, which is a joint project of the Ministério da Ciência, Tecnologia e Inovações (MCTI/LNA) do Brasil, the US National Science Foundation's NOIRLab, the University of North Carolina at Chapel Hill (UNC), and Michigan State University (MSU). This publication has made use of data collected at Lulin Observatory, partly supported by MoST grant 109-2112-M-008-001. B.E.T. acknowledges parts of this research were carried out on the traditional lands of the Ngunnawal people. We pay our respects to their elders past, present, and emerging. Based in part on data acquired at the Siding Spring Observatory 2.3 m. We acknowledge the traditional owners of the land on which the SSO stands, the Gamilaraay people, and pay our respects to elders past and present. Observations using Steward Observatory facilities were obtained as part of the large observing program AZTEC: Arizona Transient Exploration and Characterization. We are grateful to the staff at Lick Observatory for their assistance with the Nickel telescope. Research at Lick Observatory is partially supported by a generous gift from Google. The SALT data reported here were taken as part of Rutgers University program 2021-1-MLT-007 (PI: Jha). This research is based on data obtained from the Astro Data Archive at NSF's NOIRLab. These data are associated with observing programs 2012B-0001 (PI J. Frieman) and 2019B-1009 (PI P. Lira). NOIRLab is managed by the Association of Universities for Research in Astronomy (AURA) under a cooperative agreement with the National Science Foundation. This research is based on observations made with the NASA/ESA Hubble Space Telescope obtained from the Space Telescope Science Institute, which is operated by the Association of Universities for Research in Astronomy, Inc., under NASA contract NAS 5-26555. These observations are associated with program GO-6359 (PI Stiavelli; Hosseinzadeh 2022). This work is based in part on observations made with the Spitzer Space Telescope, which was operated by the Jet Propulsion Laboratory, California Institute of Technology under a contract with NASA. This work makes use of observations from the Las Cumbres Observatory network.

Time domain research by the University of Arizona team and D.J.S. is supported by NSF grants AST-1821987, 1813466, 1908972, & 2108032, and by the Heising-Simons Foundation under grant #2020-1864. Research by Y.D., N.M., and S.V. is supported by NSF grants AST-1813176 and AST-2008108. J. E.A. is supported by the international Gemini Observatory, a program of NSF's NOIRLab, which is managed by the Association of Universities for Research in Astronomy (AURA) under a cooperative agreement with the National Science Foundation, on behalf of the Gemini partnership of Argentina, Brazil, Canada, Chile, the Republic of Korea, and the United States of America. K.A.B. acknowledges support from the DIRAC Institute in the Department of Astronomy at the University of Washington. The DIRAC Institute is supported through generous gifts from the Charles and Lisa Simonyi Fund for Arts and Sciences, and the Washington Research Foundation. The Las Cumbres Observatory team is supported by NSF grants AST-1911225 and AST-1911151, and NASA Swift grant 80NSSC19K1639. The UCSC team is supported in part by the Gordon and Betty Moore Foundation, the Heising-Simons Foundation, and by a fellowship from the David and Lucile Packard Foundation to R.J.F. B.E.T. and his

group were supported by the Australian Research Council Centre of Excellence for All Sky Astrophysics in 3 Dimensions (ASTRO 3D), through project number CE170100013. P.J.B. is partially supported by NASA Astrophysics Data Analysis grant NNX17AF43G "Seeing Core-Collapse Supernovae in the Ultraviolet." C.A. and B.J.S. are supported by NASA grant 80NSSC19K1717 and NSF grants AST-1920392 and AST-1911074. L.G. and T.E.M.B. acknowledge financial support from the Spanish Ministerio de Ciencia e Innovación (MCIN), the Agencia Estatal de Investigación (AEI) 10.13039/501100011033 under the PID2020-115253GA-I00 HOSTFLOWS project, from Centro Superior de Investigaciones Científicas (CSIC) under the PIE project 20215AT016, and by the program Unidad de Excelencia María de Maeztu CEX2020-001058-M. L.G. also acknowledges MCIN, AEI and the European Social Fund (ESF) "Investing in your future" under the 2019 Ramón y Cajal program RYC2019-027683-I. M.G. is supported by the EU Horizon 2020 research and innovation program under grant agreement No. 101004719. M.N. is supported by the European Research Council (ERC) under the European Union's Horizon 2020 research and innovation program (grant agreement No. 948381) and by a Fellowship from the Alan Turing Institute.

Facilities: ADS, ARC (DIS), ATT (WiFeS), Blanco (DECam), Bok (B&C), CTIO:PROMPT, FLWO:1.2 m (KeplerCam), FTN (FLOYDS, MuSCAT3), FTS (FLOYDS), Gemini:South (GSAOI), HST (WFPC2), Keck:I (HIRES), Keck:II (KCWI, NIRES), LCOGT (Sinistro), LO:1 m (Lulin Compact Imager), Meckering:PROMPT, MMT (Binospec, MMIRS), NED, Nickel (Direct Imaging Camera), NTT (EFOSC, SOFI), OSC, SALT (RSS), Shane (Kast), SOAR (Goodman, TripleSpec), Spitzer (IRAC), Swift (UVOT), Thacher

Software: Astropy (Astropy Collaboration et al. 2018), BANZAI (McCully et al. 2018), Binospec Pipeline (Kansky et al. 2019), corner (Foreman-Mackey 2016), DoPHOT (Schechter et al. 1993), emcee (Foreman-Mackey et al. 2013), FLOYDS pipeline (Valenti et al. 2014), `hst123` (Kilpatrick et al. 2021), IPython (Perez & Granger 2007), IRAF (National Optical Astronomy Observatories 1999), `lcogtsnpipe` (Valenti et al. 2016), Light Curve Fitting (Hosseinzadeh & Gomez 2020), KCWI Data Reduction Pipeline (Rizzi et al. 2021), Matplotlib (Hunter 2007), MMIRS Pipeline (Chilingarian et al. 2013), NumPy (Oliphant 2006), `photpipe` (Rest et al. 2005), POTPyRI (K. Paterson et al. 2022, in preparation), PyKOSMOS (Davenport 2021), PyRAF (Science Software Branch at STScI 2012), PySALT (Crawford et al. 2010), PyWiFeS (Childress et al. 2014), QFitsView (Ott 2012), SciPy (Virtanen et al. 2020), `Spextool` (Cushing et al. 2004), `xtellcor` (Vacca et al. 2003).

Appendix A
Photometry Reduction

Las Cumbres Observatory images are preprocessed by BANZAI (McCully et al. 2018). We extracted aperture photometry from images taken under the Global Supernova Project using `lcogtsnpipe`, which is based on PyRAF (Science Software Branch at STScI 2012). We calibrated *UBV* magnitudes to images of Landolt (1992) standard fields (Vega magnitudes) taken on the same night with the same telescope, and we calibrated *gri* magnitudes to the Pan-STARRS1 (PS1) 3πSurvey (AB magnitudes; Chambers et al. 2016).

Las Cumbres images (including MuSCAT3) taken under the Young Supernova Experiment, as well as data from the Lulin 1 m telescope and Nickel 1 m telescope, were reduced using `photpipe` (Rest et al. 2005). *griz* magnitudes were calibrated to PS1 3π, and *u* magnitudes were calibrated to SkyMapper (Onken et al. 2019).

Thacher data were calibrated with nightly dark and bias frames and master flat-field frames in each band. We used DoPHOT (Schechter et al. 1993) to perform PSF modeling and to obtain the counts in SN 2021yja as well as 12 reference stars in the Pan-STARRS1 catalog with *r*-band magnitudes between 13.7 and 16.6 mags. Preliminary magnitudes were calculated for SN 2021yja using zero-points derived for each image based on the reference star fluxes. Then a second pass was made on the data to perform a first order color correction to account for the bandpass mismatches between the Thacher and Pan-STARRS1 filters.

Unfiltered DLT40 light curves consist of aperture photometry calibrated to *r*-band catalogs from the AAVSO Photometry All-Sky Survey (APASS; Henden et al. 2009).

Swift data were analyzed using an updated version of the pipeline for the SOUSA (Brown et al. 2014). Zero-points from Breeveld et al. (2011) were used with time-dependent sensitivity corrections updated in 2020 and an aperture correction calculated for 2021.

We perform image subtraction on each KeplerCam image with `HOTPANTS` (Becker 2015), using archival PS1 3πimages as reference templates. Instrumental magnitudes were measured using PSF fitting and calibrated to PS1 3π.

MMIRS imaging data were reduced using a custom pipeline (adapted from POTPyRI; K. Paterson et al. 2022, in preparation) that performs standard dark-current subtraction, flat-fielding, sky background estimation and subtraction, astrometric alignments, and final stacking of the individual exposures. The images were photometrically calibrated with aperture photometry of relatively isolated stars in the MMIRS images with cataloged JHK_s-band magnitudes in the Two Micron All Sky Survey (2MASS; Skrutskie et al. 2006). We then performed aperture photometry on SN 2021yja. The measurement uncertainities are dominated by scatter in the zero-point estimation from the 2MASS stars.

Appendix B
Spectroscopy Reduction

The optical and near-infrared spectra of SN 2021yja are logged in Table 5. These will be made available on the Weizmann Interactive Supernova Data Repository (Yaron & Gal-Yam 2012) after publication.

FLOYDS spectra were reduced using the FLOYDS pipeline (Valenti et al. 2014), which is based on PyRAF.

The Kast and Goodman spectra were reduced using standard IRAF/PyRAF and Python routines for bias/overscan subtractions and flat-fielding. The wavelength solution was derived using arc lamps while the final flux calibration and telluric lines removal were performed using spectrophotometric standard star spectra.

The EFOSC2 and SOFI spectra were reduced using the PESSTO pipeline (Smartt et al. 2015).

Basic 2D reductions for the MMIRS standard long-slit *zJ* single-order spectra were performed using the MMIRS data reduction pipeline (Chilingarian et al. 2013), including flat-fielding, subtraction of AB pairs to remove the sky background,

Table 5
Log of Spectroscopic Observations

MJD	Telescope	Instrument	Phase (d)	Exposure Time (s)	Wavelength Range (nm)	Resolution $\lambda/\Delta\lambda$
59466.507	FTN	FLOYDS	2.1	600	335–930	380
59466.596	FTS	FLOYDS	2.2	600	335–930	250
59467.643	FTS	FLOYDS	3.2	900	335–930	250
59467.680	SSO 2.3 m	WiFeS	3.3	3600	559–850	3000
59468.484	MMT	Binospec	4.1	1440	383–920	650
59468.769	FTS	FLOYDS	4.3	900	335–930	250
59469.480	MMT	Binospec	5.1	1440	569–721	2900
59469.606	FTS	FLOYDS	5.2	900	335–930	250
59471.312	NTT	EFOSC	6.9	900	338–932	350
59471.590	FTS	FLOYDS	7.1	900	335–930	250
59471.652	Keck II	KCWI	7.2	60	350–560	1250
59472.653	FTS	FLOYDS	8.2	1500	335–930	250
59474.485	Keck II	NIRES	10.0	1200	965–2460	2700
59474.549	FTN	FLOYDS	10.1	900	335–930	380
59475.734	FTS	FLOYDS	11.3	900	335–930	250
59476.975	SALT	RSS	12.5	1495	350–930	1000
59477.461	MMT	MMIRS	13.0	1200	940–1510	960
59477.542	FTN	FLOYDS	13.1	900	335–930	380
59478.484	FTN	FLOYDS	14.0	600	335–930	460
59479.552	FTN	FLOYDS	15.1	900	335–930	380
59479.969	SALT	RSS	15.5	1495	350–930	1000
59480.641	FTS	FLOYDS	16.1	600	335–930	270
59481.332	NTT	EFOSC	16.8	900	338–932	350
59481.961	SALT	RSS	17.5	1495	350–930	1000
59482.276	NTT	SOFI	17.8	960	950–2520	600
59482.515	FTN	FLOYDS	18.0	900	335–930	380
59483.490	Shane	Kast	19.0	630/600	300–1050	600
59483.557	FTN	FLOYDS	19.0	600	335–930	460
59486.549	FTN	FLOYDS	22.0	600	335–930	460
59487.519	FTN	FLOYDS	23.0	900	335–930	380
59488.550	FTN	FLOYDS	24.0	600	335–930	460
59490.474	FTN	FLOYDS	25.9	900	335–930	380
59490.721	FTS	FLOYDS	26.2	600	335–930	270
59492.641	FTS	FLOYDS	28.1	2400	335–930	250
59493.371	Bok	B&C	28.8	1000	601–716	3400
59494.301	Bok	B&C	29.7	1000	340–759	700
59494.634	FTS	FLOYDS	30.1	600	335–930	270
59495.760	FTS	FLOYDS	31.2	900	335–930	250
59496.726	FTS	FLOYDS	32.1	600	335–930	270
59498.522	FTN	FLOYDS	33.9	1500	335–930	380
59501.566	FTN	FLOYDS	37.0	900	335–930	380
59504.475	FTS	FLOYDS	39.8	600	335–930	270
59508.544	FTN	FLOYDS	43.9	900	335–930	380
59509.457	Keck I	HIRES	44.8	3001	364–799	50,000
59516.578	FTS	FLOYDS	51.9	600	335–930	270
59516.668	SSO 2.3 m	WiFeS	52.0	3600	350–900	3000
59517.522	FTS	FLOYDS	52.8	900	335–930	250
59517.598	SSO 2.3 m	WiFeS	52.9	3600	350–900	3000
59519.524	FTN	FLOYDS	54.8	600	335–930	460
59524.458	FTN	FLOYDS	59.7	900	335–930	380
59526.339	Shane	Kast	61.6	1703/1698	300–1050	600
59533.355	Shane	Kast	68.6	630/600	300–1050	600
59533.719	FTS	FLOYDS	68.9	900	335–930	250
59543.294	Shane	Kast	78.4	630/600	300–1050	600
59551.642	FTS	FLOYDS	86.7	900	335–930	250
59560.422	FTS	FLOYDS	95.5	900	335–930	250
59565.133	SOAR	TripleSpec	100.2	960	940–2460	3500
59565.273	MMT	MMIRS	100.3	1440	940–1510	960
59566.051	SOAR	Goodman	101.1	600	300–705	850
59566.237	MMT	MMIRS	101.3	1440	940–1510	960
59571.537	FTS	FLOYDS	106.5	900	335–930	250
59580.564	FTS	FLOYDS	115.5	900	335–930	250
59582.461	FTS	FLOYDS	117.4	1000	335–930	250

Table 5
(Continued)

MJD	Telescope	Instrument	Phase (d)	Exposure Time (s)	Wavelength Range (nm)	Resolution $\lambda/\Delta\lambda$
59586.100	Shane	Kast	121.0	630/600	300–1050	600
59593.488	FTS	FLOYDS	128.4	1000	335–930	250
59605.103	Shane	Kast	139.9	1230/1200	300–1050	600
59605.144	ARC 3.5 m	DIS	139.9	1800	380–950	1000
59611.128	Shane	Kast	145.9	930/900	300–1050	600

Note. Wavelength range and resolution are approximate. Exposure times for Kast spectra are for the blue and red halves, respectively.

and wavelength calibrations. We then performed 1D spectral extractions using standard tasks in IRAF. Flux calibrations and corrections for the strong near-infrared telluric absorption features were performed using observations of the A0V standards HD 13165, HIP 25347, and HIP 25117 taken immediately preceding each of the observations of the SN. We used the method of Vacca et al. (2003) implemented with the IDL tool `XTELLCOR_GENERAL` developed by Cushing et al. (2004) as part of the `Spextool` package.

The SALT data were reduced using a custom pipeline based on the PySALT package (Crawford et al. 2010).

Each WiFeS observation was reduced using `PyWiFeS` (Childress et al. 2014) producing a 3D cube file for each grating that has had bad pixels and cosmic rays removed, while we combined our two 1800 exposures that we took on the night. We extracted spectra from the calibrated 3D data cube using QFitsView (Ott 2012) using an aperture similar to the seeing on the night (average seeing of $1.1 - 1.6''$ on the night). For background subtraction, we extract a part of the sky that is isolated from the source using a similarly sized aperture.

Binospec data were reduced using the Binospec pipeline (Kansky et al. 2019). While an internal flux calibration into relative flux units from throughput measurements of spectrophotometric standard stars is provided in the pipeline, we obtained our own spectrophotometric standard observations throughout the semester and created our own sensitivty function for flux calibration.

Reductions of Bok B&C spectra were carried out using IRAF including bias subtraction, flat fielding, and optimal extraction of the spectra. Flux calibration was achieved using spectrophotometric standards observed at an air mass similar to that of each science frame, and the resulting spectra were median combined into a single 1D spectrum for each epoch.

The DIS spectrum was reduced using PyKOSMOS (Davenport 2021) using standard techniques for bias/overscan subtraction, flat-field correction, 1D extraction, and wavelength calibration. Flux calibration was performed using the optical flux standard star LTT2415. 1D observations were cleaned and median combined to produce the final spectrum.

The HIRES spectra were reduced using the standard procedure of the California Planet Search (Howard et al. 2010). We extracted the two orders of interest, containing the DIB and the Na I D lines. For each order, we median-combined the four exposures, masked the lines of interest, and then modeled the continuum by smoothing with a second-order Savitzky & Golay (1964) filter with a width of 555 pixels. Figure 5 shows this spectrum divided by the continuum.

The KCWI spectra were reduced following the standard procedures used in the python version of the KCWI Data Reduction Pipeline (Rizzi et al. 2021). The spectra were extracted from the data cube using QFitsView (Ott 2012).

The NIRES spectrum was reduced following standard procedures described in the IDL package `Spextool` version 5.0.2 for NIRES (Cushing et al. 2004). The extracted 1D spectrum was flux calibrated and also corrected for telluric features with `xtellcorr` version 5.0.2 for NIRES (Vacca et al. 2003) making use of observations of an A0V standard star.

We used the `Spextool` IDL package (Cushing et al. 2004) to reduce the TripleSpec data, and we subtracted consecutive AB pairs to remove the sky and the dark current. The pixel-to-pixel gain variations in the science frames were corrected by dividing for the normalized master flat. We calibrated 2D science frames in wavelength by using CuHeAr Hollow Cathode comparison lamps. To correct for telluric features and to flux-calibrate the SN spectra, we observed the HIP 19001 A0V telluric standard after the SN and at a similar air mass. After the extraction of the individual spectra from the 2D frames, we used the `xtellcorr` task (Vacca et al. 2003) included in the `Spextool` IDL package to perform the telluric correction and the flux calibration.

ORCID iDs

Griffin Hosseinzadeh https://orcid.org/0000-0002-0832-2974
Charles D. Kilpatrick https://orcid.org/0000-0002-5740-7747
Yize Dong (董一泽) https://orcid.org/0000-0002-7937-6371
David J. Sand https://orcid.org/0000-0003-4102-380X
Jennifer E. Andrews https://orcid.org/0000-0003-0123-0062
K. Azalee Bostroem https://orcid.org/0000-0002-4924-444X
Daryl Janzen https://orcid.org/0000-0003-0549-3281
Jacob E. Jencson https://orcid.org/0000-0001-5754-4007
Michael Lundquist https://orcid.org/0000-0001-9589-3793
Nicolas E. Meza Retamal https://orcid.org/0000-0002-7015-3446
Jeniveve Pearson https://orcid.org/0000-0002-0744-0047
Stefano Valenti https://orcid.org/0000-0001-8818-0795
Samuel Wyatt https://orcid.org/0000-0003-2732-4956
Jamison Burke https://orcid.org/0000-0003-0035-6659
Daichi Hiramatsu https://orcid.org/0000-0002-1125-9187
D. Andrew Howell https://orcid.org/0000-0003-4253-656X
Curtis McCully https://orcid.org/0000-0001-5807-7893
Estefania Padilla Gonzalez https://orcid.org/0000-0003-0209-9246
Craig Pellegrino https://orcid.org/0000-0002-7472-1279

Giacomo Terreran https://orcid.org/0000-0003-0794-5982
Katie Auchettl https://orcid.org/0000-0002-4449-9152
Kyle W. Davis https://orcid.org/0000-0002-5680-4660
Ryan J. Foley https://orcid.org/0000-0002-2445-5275
Hao-Yu Miao (繆皓宇) https://orcid.org/0000-0003-2736-5977
Yen-Chen Pan (潘彥丞) https://orcid.org/0000-0001-8415-6720
Armin Rest https://orcid.org/0000-0002-4410-5387
Matthew R. Siebert https://orcid.org/0000-0003-2445-3891
Kirsty Taggart https://orcid.org/0000-0002-5748-4558
Brad E. Tucker https://orcid.org/0000-0002-4283-5159
Feng Lin Cyrus Leung https://orcid.org/0000-0002-6604-8838
Jonathan J. Swift https://orcid.org/0000-0002-9486-818X
Grace Yang https://orcid.org/0000-0001-7823-2627
Joseph P. Anderson https://orcid.org/0000-0003-0227-3451
Chris Ashall https://orcid.org/0000-0002-5221-7557
Stefano Benetti https://orcid.org/0000-0002-3256-0016
Peter J. Brown https://orcid.org/0000-0001-6272-5507
Régis Cartier https://orcid.org/0000-0003-4553-4033
Ting-Wan Chen (陳婷琬) https://orcid.org/0000-0002-1066-6098
Massimo Della Valle https://orcid.org/0000-0003-3142-5020
Lluís Galbany https://orcid.org/0000-0002-1296-6887
Sebastian Gomez https://orcid.org/0000-0001-6395-6702
Mariusz Gromadzki https://orcid.org/0000-0002-1650-1518
Joshua Haislip https://orcid.org/0000-0002-6703-805X
Eric Y. Hsiao https://orcid.org/0000-0003-1039-2928
Cosimo Inserra https://orcid.org/0000-0002-3968-4409
Saurabh W. Jha https://orcid.org/0000-0001-8738-6011
Thomas L. Killestein https://orcid.org/0000-0002-0440-9597
Vladimir Kouprianov https://orcid.org/0000-0003-3642-5484
Alexandra Kozyreva https://orcid.org/0000-0001-9598-8821
Tomás E. Müller-Bravo https://orcid.org/0000-0003-3939-7167
Matt Nicholl https://orcid.org/0000-0002-2555-3192
Emmy Paraskeva https://orcid.org/0000-0003-2814-4383
Daniel E. Reichart https://orcid.org/0000-0002-5060-3673
Stuart Ryder https://orcid.org/0000-0003-4501-8100
Melissa Shahbandeh https://orcid.org/0000-0002-9301-5302
Ben Shappee https://orcid.org/0000-0003-4631-1149
Nathan Smith https://orcid.org/0000-0001-5510-2424
David R. Young https://orcid.org/0000-0002-1229-2499

References

Abdalla, H., Aharonian, F., Benkhali, F. A., et al. 2019, A&A, 626, A57
Alsaberi, R. Z. E., Ryder, S. D., Marnoch, L., et al. 2021, ATel, 14942, 1
Anderson, J. P. 2019, A&A, 628, A7
Anderson, J. P., González-Gaitán, S., Hamuy, M., et al. 2014, ApJ, 786, 67
Andrews, J. E., Sand, D. J., Valenti, S., Smith, N., & Dastidar, R. 2019, ApJ, 855, 43
Astropy Collaboration, Price-Whelan, A. M., Sipőcz, B. M., et al. 2018, AJ, 156, 123
Barbon, R., Ciatti, F., & Rosino, L. 1979, A&A, 72, 287
Beasor, E. R., Davies, B., Smith, N., et al. 2020, MNRAS, 492, 5994
Becker, A. 2015, HOTPANTS: High Order Transform of PSF ANd Template Subtraction, Astrophysics Source Code Library, ascl:1504.004
Bellm, E. C., Kulkarni, S. R., Graham, M. J., et al. 2019, PASP, 131, 018002
Blondin, S., & Tonry, J. L. 2007, ApJ, 666, 1024
Boian, I., & Groh, J. H. 2020, MNRAS, 496, 1325
Bose, S., Kumar, B., Sutaria, F., et al. 2013, MNRAS, 433, 1871
Bostroem, K. A., Valenti, S., Horesh, A., et al. 2019, MNRAS, 485, 5120
Bostroem, K. A., Valenti, S., Sand, D. J., et al. 2020, ApJ, 895, 31
Breeveld, A. A., Landsman, W., Holland, S. T., et al. 2011, in AIP Conf. Proc. 1358, GAMMA RAY BURSTS 2010 (New York: AIP), 373
Brown, P. J., Breeveld, A. A., Holland, S., Kuin, P., & Pritchard, T. 2014, Ap&SS, 354, 89
Brown, T. M., Baliber, N., Bianco, F. B., et al. 2013, PASP, 125, 1031
Bruch, R. J., Gal-Yam, A., Schulze, S., et al. 2021, ApJ, 912, 46
Bullivant, C., Smith, N., Williams, G. G., et al. 2018, MNRAS, 476, 1497
Buzzoni, B., Delabre, B., Dekker, H., et al. 1984, Msngr, 38, 9
Cao, Y., Kasliwal, M. M., Arcavi, I., et al. 2013, ApJ, 775, L7
Catchpole, R. M., Whitelock, P. A., Feast, M. W., et al. 1988, MNRAS, 231, 75P
Chambers, K. C., Magnier, E. A., Metcalfe, N., et al. 2016, arXiv:1612.05560
Childress, M. J., Vogt, F. P. A., Nielsen, J., & Sharp, R. G. 2014, Ap&SS, 349, 617
Chilingarian, I., Brown, W., Fabricant, D., et al. 2013, in ASP Conf. Ser. 475, Astronomical Data Analysis Software and Systems XXII (San Francisco, CA: ASP), 189
Choi, J., Dotter, A., Conroy, C., et al. 2016, ApJ, 823, 102
Clemens, J. C., Crain, J. A., & Anderson, R. 2004, Proc. SPIE, 5492, 331
Colgate, S. A., & McKee, C. 1969, ApJ, 157, 623
Conroy, C., Strader, J., van Dokkum, P., et al. 2018, ApJ, 864, 111
Crawford, S. M., Still, M., Schellart, P., et al. 2010, Proc. SPIE, 7737, 25
Cushing, M. C., Vacca, W. D., & Rayner, J. T. 2004, PASP, 116, 362
Dall'Ora, M., Botticella, M. T., Pumo, M. L., et al. 2014, ApJ, 787, 139
Davenport, J. 2021, PyKOSMOS: A Python-Based Spectral Reduction Suite for KOSMOS at APO v1, Zenodo doi:10.5281/zenodo.5120786
Davies, B., & Beasor, E. R. 2018, MNRAS, 474, 2116
Davies, B., & Beasor, E. R. 2020a, MNRAS, 496, L142
Davies, B., & Beasor, E. R. 2020b, MNRAS, 493, 468
Davis, S., Hsiao, E. Y., Ashall, C., et al. 2019, ApJ, 887, 4
de Jaeger, T., Zheng, W., Stahl, B. E., et al. 2019, MNRAS, 490, 2799
Deckers, M., Dimitriadis, G., Harvey, L., Terwel, J., & Yaron, O. 2021a, TNSCR, 3183, 1
Deckers, M., Dimitriadis, G., Terwel, J., et al. 2021b, TNSAN, 242, 1
Dessart, L., & Hillier, D. J. 2005, A&A, 439, 671
Dessart, L., Hillier, D. J., & Audit, E. 2017, A&A, 605, A83
Dong, Y., Valenti, S., Bostroem, K. A., et al. 2021, ApJ, 906, 56
Dopita, M., Hart, J., McGregor, P., et al. 2007, Ap&SS, 310, 255
Dopita, M., Rhee, J., Farage, C., et al. 2010, Ap&SS, 327, 245
Eastman, R. G., Schmidt, B. P., & Kirshner, R. 1996, ApJ, 466, 911
Eldridge, J. J., Guo, N.-Y., Rodrigues, N., Stanway, E. R., & Xiao, L. 2019, PASA, 36, e041
Elmhamdi, A., Danziger, I. J., Chugai, N., et al. 2003, MNRAS, 338, 939
Fabricant, D., Fata, R., Epps, H., et al. 2019, PASP, 131, 075004
Falcón-Barroso, J., Lyubenova, M., van de Ven, G., et al. 2017, A&A, 597, A48
Faran, T., Goldfriend, T., Nakar, E., & Sari, R. 2019, ApJ, 879, 20
Faran, T., Poznanski, D., Filippenko, A. V., et al. 2014, MNRAS, 442, 844
Fazio, G. G., Hora, J. L., Allen, L. E., et al. 2004, ApJS, 154, 10
Fitzpatrick, E. L. 1999, PASP, 111, 63
Foreman-Mackey, D. 2016, JOSS, 1, 24
Foreman-Mackey, D., Hogg, D. W., Lang, D., & Goodman, J. 2013, PASP, 125, 306
Förster, F., Moriya, T. J., Maureira, J. C., et al. 2018, NatAs, 2, 808
Gal-Yam, A., Arcavi, I., Ofek, E. O., et al. 2014, Natur, 509, 471
Galbany, L., Hamuy, M., Phillips, M. M., et al. 2016, AJ, 151, 33
Gehrels, N., Chincarini, G., Giommi, P., et al. 2004, ApJ, 611, 1005
Gehrz, R. D., Roellig, T. L., Werner, M. W., et al. 2007, RScI, 78, 011302
Goldberg, J. A., Bildsten, L., & Paxton, B. 2019, ApJ, 879, 3
González-Gaitán, S., Tominaga, N., Molina, J., et al. 2015, MNRAS, 451, 2212
Green, R., Schmidt, G., Oey, S., Wittman, D., & Hall, P. 1995, Steward Observatory 2.3-m Boller and Chivens Spectrograph Manual, https://james.as.arizona.edu/psmith/90inch/bcman/html/bcman.html
Guidi, G., Casado, J., Ascasibar, Y., et al. 2018, MNRAS, 479, 917
Guillochon, J., Parrent, J., Kelley, L. Z., & Margutti, R. 2017, ApJ, 835, 64
Hamuy, M., Pinto, P. A., Maza, J., et al. 2001, ApJ, 558, 615
H.E.S.S. Collaboration, Abdalla, H., Aharonian, F., et al. 2022, ICRC (Berlin), 37, 809
Henden, A. A., Welch, D. L., Terrell, D., & Levine, S. E. 2009, AAS, 41, 407.02

Hiramatsu, D., Howell, D. A., Moriya, T. J., et al. 2021a, ApJ, 913, 55
Hiramatsu, D., Howell, D. A., Van Dyk, S. D., et al. 2021b, NatAs, 5, 903
Hodgkin, S. T., Breedt, E., Delgado, A., et al. 2021, TNSTR, 4190, 1
Hosseinzadeh, G. 2022, HST Imaging of NGC 1325, STScI/MAST,
Hosseinzadeh, G., & Gomez, S. 2020, Light Curve Fitting v0.2.0, Zenodo, doi:10.5281/zenodo.4312178
Hosseinzadeh, G., Valenti, S., McCully, C., et al. 2018, ApJ, 861, 63
Howard, A. W., Johnson, J. A., Marcy, G. W., et al. 2010, ApJ, 721, 1467
Howell, D. A., Sullivan, M., Perrett, K., et al. 2005, ApJ, 634, 1190
Hunter, J. D. 2007, CSE, 9, 90
Jacobson-Galán, W. V., Dessart, L., Jones, D. O., et al. 2022, ApJ, 924, 15
Jencson, J. E., Sand, D. J., Andrews, J. E., et al. 2022, ApJ, 930, 81
Jones, D. O., Foley, R. J., Narayan, G., et al. 2021, ApJ, 908, 143
Jones, M. I., Hamuy, M., Lira, P., et al. 2009, ApJ, 696, 1176
Jordi, K., Grebel, E. K., & Ammon, K. 2006, A&A, 460, 339
Kansky, J., Chilingarian, I., Fabricant, D., et al. 2019, PASP, 131, 075005
Kasen, D., & Woosley, S. E. 2009, ApJ, 703, 2205
Khazov, D., Yaron, O., Gal-Yam, A., et al. 2016, ApJ, 818, 3
Kilpatrick, C. D. 2021, TNSAN, 236, 1
Kilpatrick, C. D., Drout, M. R., Auchettl, K., et al. 2021, MNRAS, 504, 2073
Kilpatrick, C. D., Foley, R. J., Drout, M. R., et al. 2018, MNRAS, 473, 4805
Kirshner, R. P., & Kwan, J. 1974, ApJ, 193, 27
Kozyreva, A., Nakar, E., Waldman, R., Blinnikov, S., & Baklanov, P. 2020, MNRAS, 494, 3927
Landolt, A. U. 1992, AJ, 104, 340
Leonard, D. C., Filippenko, A. V., Gates, E. L., et al. 2002, PASP, 114, 35
Levesque, E. M. 2017, Astrophysics of Red Supergiants (Bristol: IOP Publishing)
Levesque, E. M., & Massey, P. 2020, ApJL, 891, L37
Li, W., Leaman, J., Chornock, R., et al. 2011, MNRAS, 412, 1441
Lupton, R. 2005, DIS: The Double Imaging Spectrograph, https://www.apo.nmsu.edu/35m_operations/35m_manual/Instruments/DIS/DIS_usage.html#Lupton_Manual
Martinez, L., Bersten, M. C., Anderson, J. P., et al. 2022, A&A, 660, A40
Martinez, L., Pessi, P., Ertini, K., Ferrari, L., & Folatelli, G. 2021, TNSAN, 237, 1
McCully, C., Volgenau, N., Harbeck, D. R., et al. 2018, Proc. SPIE, 10707, 107070K
McGregor, P., Hart, J., Stevanovic, D., et al. 2004, Proc. SPIE, 5492, 1033
McLeod, B., Fabricant, D., Nystrom, G., et al. 2012, PASP, 124, 1318
Miller, J. S., & Stone, R. P. S. 1994, The Kast Double Spectrograph, Tech. Rep., 66 Lick Observatory
Moorwood, A., Cuby, J. G., & Lidman, C. 1998, Msngr, 91, 9
Morozova, V., Piro, A. L., Fuller, J., & Dyk, S. D. V. 2020, ApJ, 891, L32
Morozova, V., Piro, A. L., & Valenti, S. 2017, ApJ, 838, 28
Morozova, V., Piro, A. L., & Valenti, S. 2018, ApJ, 858, 15
Morrissey, P., Matuszewski, M., Martin, D. C., et al. 2018, ApJ, 864, 93
Munari, U., Henden, A., Belligoli, R., et al. 2013, NewA, 20, 30
Munari, U., & Zwitter, T. 1997, A&A, 318, 269
Nakar, E., & Sari, R. 2010, ApJ, 725, 904
Narita, N., Fukui, A., Yamamuro, T., et al. 2020, Proc. SPIE, 11447, 114475K
National Optical Astronomy Observatories 1999, IRAF: Image Reduction and Analysis Facility, Astrophysics Source Code Library, ascl:9911.002
Oliphant, T. E. 2006, A Guide to NumPy (USA: Trelgol Publishing), http://www.trelgol.com/
Onken, C. A., Wolf, C., Bessell, M. S., et al. 2019, PASA, 36, e033
Ott, T. 2012, QFitsView: FITS File Viewer, Astrophysics Source Code Library, ascl:1210.019
Pellegrino, C., Burke, J., Hiramatsu, D., et al. 2021, TNSCR, 3115, 1
Perez, F., & Granger, B. E. 2007, CSE, 9, 21
Phillips, M. M., Simon, J. D., Morrell, N., et al. 2013, ApJ, 779, 38
Planck, M. 1906, Vorlesungen Über die Theorie der Wärmestrahlung (Leipzig: J. A. Barth) https://ia804507.us.archive.org/12/items/uberdietheoewarm00planrich/uberdietheoewarm00planrich.pdf
Planck Collaboration, Aghanim, N., Akrami, Y., et al. 2020, A&A, 641, A6
Popov, D. V. 1993, ApJ, 414, 712
Poznanski, D., Prochaska, J. X., & Bloom, J. S. 2012, MNRAS, 426, 1465
Reichart, D., Nysewander, M., Moran, J., et al. 2005, NCimC, 28, 767
Rest, A., Stubbs, C., Becker, A. C., et al. 2005, ApJ, 634, 1103
Richmond, M. W., Treffers, R. R., Filippenko, A. V., et al. 1994, AJ, 107, 1022
Rizzi, L., Neill, D., & Brodheim, M. 2021, Keck Cosmic Web Imager Data Reduction Pipeline, https://github.com/Keck-DataReductionPipelines/KCWI_DRP
Roming, P. W. A., Kennedy, T. E., Mason, K. O., et al. 2005, SSRv, 120, 95
Rubin, A., & Gal-Yam, A. 2017, ApJ, 848, 8
Rubin, A., Gal-Yam, A., Cia, A. D., et al. 2016, ApJ, 820, 33
Ryder, S. D., Marnoch, L., Kundu, E., et al. 2021, ATel, 14915, 1
Sapir, N., & Waxman, E. 2017, ApJ, 838, 130
Savitzky, A., & Golay, M. J. E. 1964, AnaCh, 36, 1627
Schechter, P. L., Mateo, M., & Saha, A. 1993, PASP, 105, 1342
Schlafly, E. F., & Finkbeiner, D. P. 2011, ApJ, 737, 103
Schlafly, E. F., Finkbeiner, D. P., Schlegel, D. J., et al. 2010, ApJ, 725, 1175
Schlawin, E., Herter, T. L., Henderson, C., et al. 2014, Proc. SPIE, 9147, 91472H
Science Software Branch at STScI 2012, PyRAF: Python Alternative for IRAF, Astrophysics Source Code Library, ascl:1207.011
Shappee, B. J., Prieto, J. L., Grupe, D., et al. 2014, ApJ, 788, 48
Shussman, T., Waldman, R., & Nakar, E. 2016, arXiv:1610.05323
Skrutskie, M. F., Cutri, R. M., Stiening, R., et al. 2006, AJ, 131, 1163
Smartt, S. J. 2015, PASA, 32, e016
Smartt, S. J., Valenti, S., Fraser, M., et al. 2015, A&A, 579, A40
Smith, K. W., Smartt, S. J., Young, D. R., et al. 2020, PASP, 132, 085002
Smith, K. W., Srivastav, S., Smartt, S. J., et al. 2021, TNSAN, 235, 1
Smith, M. P., Nordsieck, K. H., Burgh, E. B., et al. 2006, Proc. SPIE, 6269, 2A
Smith, N. 2014, ARA&A, 52, 487
Smith, N., & Arnett, W. D. 2014, ApJ, 785, 82
Smith, N., Li, W., Filippenko, A. V., & Chornock, R. 2011, MNRAS, 412, 1522
Smith, N., Mauerhan, J. C., Cenko, S. B., et al. 2015, MNRAS, 449, 1876
Soraisam, M. D., Bildsten, L., Drout, M. R., et al. 2018, ApJ, 859, 73
Soumagnac, M. T., Ganot, N., Irani, I., et al. 2020, ApJ, 902, 6
Spiro, S., Pastorello, A., Pumo, M. L., et al. 2014, MNRAS, 439, 2873
Springob, C. M., Haynes, M. P., Giovanelli, R., & Kent, B. R. 2005, ApJS, 160, 149
Stone, R. P. S., & Shields, J. 1990, The CCD Spectrograph and Camera at the Nickel Telescope, Tech. Rep., 52 Lick Observatory
Swift, J. J., Andersen, K., Arculli, T., et al. 2022, PASP, 134, 035005
Szalai, T., Vinkó, J., Könyves-Tóth, R., et al. 2019, ApJ, 876, 19
Szentgyorgyi, A. H., Geary, J. G., Latham, D. W., et al. 2005, AAS Meeting, 207, 110.10
Tartaglia, L., Sand, D. J., Groh, J. H., et al. 2021, ApJ, 907, 52
Tartaglia, L., Sand, D. J., Valenti, S., et al. 2018, ApJ, 853, 62
Terreran, G., Jacobson-Galán, W. V., Groh, J. H., et al. 2022, ApJ, 926, 20
Tonry, J., Denneau, L., Heinze, A., et al. 2021, TNSTR, 3093, 1
Tonry, J. L., Denneau, L., Heinze, A. N., et al. 2018a, PASP, 130, 064505
Tonry, J., Stalder, B., Denneau, L., et al. 2018b, TNSTR, 707, 1
Tuairisg, S. Ó, Cami, J., Foing, B. H., Sonnentrucker, P., & Ehrenfreund, P. 2000, A&AS, 142, 225
Tully, R. B., Courtois, H. M., & Sorce, J. G. 2016, AJ, 152, 50
Tully, R. B., & Fisher, J. R. 1977, A&A, 54, 661
Vacca, W. D., Cushing, M. C., & Rayner, J. T. 2003, PASP, 115, 389
Valenti, S., Howell, D. A., Stritzinger, M. D., et al. 2016, MNRAS, 459, 3939
Valenti, S., Sand, D., Pastorello, A., et al. 2014, MNRAS, 438, L101
Van Dyk, S. D. 2016, in Handbook of Supernovae, ed. A. W. Alsabti & P. Murdin (Cham: Springer),
Vasylyev, S. S., Filippenko, A. V., Vogl, C., et al. 2022, arXiv:2203.08001
Virtanen, P., Gommers, R., Oliphant, T. E., et al. 2020, NatMe, 17, 261
Vogt, S. S., Allen, S. L., Bigelow, B. C., et al. 1994, Proc. SPIE, 2198, 362
Wegner, G. 1977, MNRAS, 181, 677
Werner, M. W., Roellig, T. L., Low, F. J., et al. 2004, ApJS, 154, 1
Williamson, M., Modjaz, M., Pellegrino, C., et al. 2021, TNSCR, 3130, 1
Wilson, J. C., Henderson, C. P., Herter, T. L., et al. 2004, Proc. SPIE, 5492, 1295
Yaron, O., & Gal-Yam, A. 2012, PASP, 124, 668
Yaron, O., Perley, D. A., Gal-Yam, A., et al. 2017, NatPh, 13, 510